The Astrophysical Journal Letters, 939:L7 (8pp), 2022 November 1 https://doi.org/10.3847/2041-8213/ac98c6


# JWST Sneaks a Peek at the Stellar Morphology of $z \sim 2$ Submillimeter Galaxies: Bulge Formation at Cosmic Noon

Chian-Chou Chen (陳建州)[1], Zhen-Kai Gao[1,2], Qi-Ning Hsu[1,3], Cheng-Lin Liao[1,3], Yu-Han Ling[1], Ching-Min Lo[1], Ian Smail[4], Wei-Hao Wang[1], and Yu-Jan Wang[1]
[1] Academia Sinica Institute of Astronomy and Astrophysics (ASIAA), No. 1, Section 4, Roosevelt Road, Taipei 10617, Taiwan; ccchen@asiaa.sinica.edu.tw
[2] Graduate Institute of Astronomy, National Central University, 300 Zhongda Road, Zhongli, Taoyuan 32001, Taiwan
[3] Graduate Institute of Astrophysics, National Taiwan University, Taipei 10617, Taiwan
[4] Centre for Extragalactic Astronomy, Department of Physics, Durham University, South Road, Durham DH1 3LE, UK
*Received 2022 August 10; revised 2022 October 7; accepted 2022 October 8; published 2022 October 27*

## Abstract

We report morphological analyses of seven submillimeter galaxies (SMGs) at $z \sim 2$ using the James Webb Space Telescope NIRCam images taken as part of the public CEERS and PRIMER surveys. Through two-dimensional surface brightness profile fitting we find evidence of compact reddened stellar structures in all the SMGs, in particular in the F444W filter, suggesting an ubiquitous presence of stellar bulges. The median size of these bulges at F444W with a bootstrapped uncertainty is found to be $0.7 \pm 1.0$ kpc (0.6–0.7–3.9 kpc for 14th–50th–86th percentiles) and the median Sérsic index is $0.7 \pm 0.9$ (0.4–0.7–2.8 for 14th–50th–86th percentiles). Structures akin to spiral arms and bars are also identified, and their asymmetric shapes, tidal features, as well as evidence of nearby galaxies at consistent redshifts as those of corresponding SMGs suggest that these SMGs are undergoing dynamical interactions, likely responsible for the triggering of their star-forming activity. Via a curve-of-growth analysis we deduce half-light radii for the NIRCam wave bands, finding that sizes are significantly smaller at longer wavelengths in all cases, in particular that the median size ratio between F444W and F150W is $0.6 \pm 0.1$. However, we also find that F444W sizes, roughly corresponding to rest-frame *H* band, are not smaller than those of submillimeter continuum as measured by the Atacama Large Millimeter/submillimeter Array, contradicting certain recent predictions from theoretical models. Our results suggest that while stellar bulges are undergoing an active formation phase in SMGs at $z \sim 2$, the total stellar masses of SMGs are still dominated by their disks, not bulges.

*Unified Astronomy Thesaurus concepts:* High-redshift galaxies (734); Galaxy structure (622); Ultraluminous infrared galaxies (1735); Galaxy interactions (600); Galaxy formation (595)

## 1. Introduction

The epoch of $z \sim 1$–3, so called the cosmic noon, represents a key phase of rapid stellar mass assembly for massive galaxies, and this active formation phase is now known to mostly take place in galaxies that are infrared luminous (Madau & Dickinson 2014). These dusty infrared luminous star-forming galaxies are often detected via submillimeter observations (Smail et al. 1997; Barger et al. 1998; Hughes et al. 1998; Blain et al. 2002; Casey et al. 2014), and these submillimeter galaxies (SMGs) are massive systems at cosmic noon (e.g., Chapman et al. 2005; Danielson et al. 2017; Chen et al. 2022) that are believed to intimately link to compact quiescent galaxies at similar redshifts and the formation of massive local ellipticals (Lilly et al. 1999; Toft et al. 2014; Dudzevičiūtė et al. 2020). Given their important role in galaxy evolution, exactly how SMGs build up their stellar mass is one key question to galaxy formation models.

Recent observational studies have shown almost ubiquitously that the sizes of the submillimeter continuum of SMGs are compact, about 1–2 kpc (Ikarashi et al. 2015; Simpson et al. 2015; Hodge et al. 2016; Spilker et al. 2016; Fujimoto et al. 2018; Gullberg et al. 2019). The submillimeter sizes are also found to be smaller than those deduced from optical and near-infrared continuum images (Chen et al. 2015; Fujimoto et al. 2018; Lang et al. 2019) or emission lines (Calistro Rivera et al. 2018; Chen et al. 2020), typically by a factor of 2–3. This evidence suggests that SMGs are actively forming stars in the central regions and the stellar bulges have been quickly built up. Bulge formation, or similarly the inside-out growth scenario, has been suggested from various studies for massive galaxies at cosmic noon (e.g., Nelson et al. 2016; Tadaki et al. 2020), and has been predicted also by recent theoretical models (e.g., Cochrane et al. 2019; Popping et al. 2022). However, due to heavy dust obscuration, observational evidence of the presence of stellar bulges in SMGs has been an indirect one, including those inferred from the observed colors (Lang et al. 2019). Stellar size measurements on massive galaxies at cosmic noon in general have also been found to be significantly affected by dust obscuration. Recent studies using color information have suggested that the true stellar sizes are significantly smaller than what have been inferred from Hubble Space Telescope (HST) *H*-band studies (Suess et al. 2019; Miller et al. 2022).

On the other hand, heavy dust obscuration has also hampered our ability to determine the triggering mechanism of star formation in SMGs using HST images, where often times it is not possible to distinguish irregular disks and mergers (Swinbank et al. 2010; Mortlock et al. 2013; Chang et al. 2018). However the dominant triggering mechanism of star formation for SMGs has been a key factor that differentiates various theoretical models (Baugh et al. 2005; Davé et al. 2010; Hayward et al. 2013; Cowley et al. 2015; Lagos et al. 2020), making a definite determination on this

**Table 1**
Properties of the Sample SMGs and Their Measured Sizes

| ID[a] | $S_{850/870}$[b] (mJy) | $z$[c] | $\log(M_*)$[c] ($M_\odot$) | $\log(L_{IR})$[c] ($L_\odot$) | $R_{e,F115W}$[d] (kpc) | $R_{e,F150W}$[d] (kpc) | $R_{e,F200W}$[d] (kpc) | $R_{e,F277W}$[d] (kpc) | $R_{e,F356W}$[d] (kpc) | $R_{e,F444W}$[d] (kpc) |
|---|---|---|---|---|---|---|---|---|---|---|
| 850.017 | $2.7 \pm 0.4$ | $2.37^{+0.00}_{-0.02}$ | $11.3 \pm 0.3$ | $12.6 \pm 0.1$ | $8.1^{+0.6}_{-0.6}$ | $7.7^{+0.4}_{-0.4}$ | $6.1^{+0.2}_{-0.2}$ | $5.3^{+0.3}_{-0.3}$ | $4.6^{+0.2}_{-0.2}$ | $4.1^{+0.2}_{-0.2}$ |
| 850.019 | $3.4 \pm 0.5$ | $2.33^{+0.01}_{-0.01}$ | $10.7 \pm 0.1$ | $12.3 \pm 0.1$ | ⋯ | $6.5^{+0.4}_{-0.4}$ | $6.0^{+0.3}_{-0.3}$ | $5.2^{+0.4}_{-0.4}$ | $4.9^{+0.3}_{-0.3}$ | $4.7^{+0.2}_{-0.2}$ |
| 850.025 | $2.7 \pm 0.3$ | $2.14^{+0.03}_{-0.01}$ | $11.3 \pm 0.1$ | $11.9 \pm 0.1$ | $5.9^{+0.7}_{-0.7}$ | $5.3^{+0.3}_{-0.3}$ | $5.0^{+0.2}_{-0.2}$ | $4.7^{+0.2}_{-0.3}$ | $4.4^{+0.2}_{-0.2}$ | $4.3^{+0.2}_{-0.2}$ |
| 850.030 | $2.1 \pm 0.4$ | $1.74^{+0.01}_{-0.19}$ | $11.4 \pm 0.1$ | $11.9 \pm 0.1$ | $11.3^{+0.7}_{-0.7}$ | $10.3^{+0.7}_{-0.7}$ | $7.8^{+0.8}_{-0.8}$ | $6.7^{+0.8}_{-0.8}$ | $6.1^{+0.8}_{-0.7}$ | $5.8^{+0.7}_{-0.7}$ |
| 850.038 | $2.1 \pm 0.4$ | $1.93^{+0.09}_{-0.01}$ | $10.9 \pm 0.1$ | $11.9 \pm 0.1$ | ⋯ | $5.0^{+0.3}_{-0.3}$ | ⋯ | $4.7^{+0.3}_{-0.3}$ | $4.2^{+0.2}_{-0.2}$ | $3.9^{+0.2}_{-0.2}$ |
| 850.043 | $1.7 \pm 0.4$ | $1.51^{+0.01}_{-0.01}$ | $10.9 \pm 0.1$ | $11.9 \pm 0.1$ | $3.0^{+0.3}_{-0.3}$ | $2.6^{+0.1}_{-0.1}$ | $2.2^{+0.1}_{-0.1}$ | $1.8^{+0.1}_{-0.1}$ | $1.6^{+0.1}_{-0.1}$ | $1.6^{+0.1}_{-0.1}$ |
| AS2UDS.125.0 | $4.6 \pm 0.5$ | 2.154 | $11.7 \pm 0.1$ | $12.5 \pm 0.1$ | $7.0^{+0.7}_{-0.7}$ | $7.1^{+0.3}_{-0.3}$ | $5.2^{+0.1}_{-0.1}$ | $5.1^{+0.2}_{-0.2}$ | $4.6^{+0.1}_{-0.1}$ | $4.5^{+0.1}_{-0.1}$ |

**Notes.**
[a] IDs adopted from Zavala et al. (2017), except for AS2UDS.125.0, which is based on Stach et al. (2019).
[b] Deboosted 850 $\mu$m flux densities measured from SCUBA-2 as reported by Zavala et al. (2017), except for AS2UDS.125.0, where its 870 $\mu$m flux density was reported by Stach et al. (2019).
[c] Redshifts, stellar masses, and infrared luminosities adopted from Zavala et al. (2018), except AS2UDS.125.0, for which its properties are adopted from Lang et al. (2019). The redshifts with quoted uncertainties are photometric, otherwise spectroscopic.
[d] Half-light radii ($R_e$) are estimated along the semimajor axis from the curve-of-growth analyses (Section 3.2).

issue would make a major step forward in modeling SMGs, as well as the formation of massive galaxies in general.

With the advent of James Webb Space Telescope (JWST), its sensitive high-resolution observations at mid-infrared allow us to finally be able to directly image rest-frame near-infrared morphologies at subkiloparsec scales for galaxies at cosmic noon, revealing stellar components that are previously hidden in images at shorter wavelengths. Indeed, early results from JWST have found that the mid-infrared sizes are smaller than those of previous HST $H$-band observations (Cheng et al. 2022; Suess et al. 2022), suggesting a significant amount of missing stellar emissions in the central regions in previous HST measurements.

In this Letter we study stellar distributions of SMGs at $z \sim 2$ using JWST images. We describe sample selection and data in Section 2. We present our analyses and results in Section 3, and finally discussion and summary are given in Section 4. Throughout this Letter we assume the Planck cosmology: $H_0 = 67.7\,\mathrm{km\,s^{-1}\,Mpc^{-1}}$, $\Omega_M = 0.31$, and $\Omega_\Lambda = 0.69$ (Planck Collaboration et al. 2020).

## 2. Observations and Data

### 2.1. Sample

Our SMG sample is based on the 850 $\mu$m SCUBA-2 Cosmological Survey (S2CLS; Geach et al. 2017) in the Extended Groth Strip (EGS) and UKIDSS-Ultra Deep Survey (UDS) fields, where the flux limits are $\sim$1 and 3.4 mJy, respectively. For the EGS field, the number counts, counterpart identifications, and detailed studies of the physical properties of the submillimeter sources have been performed and presented in Zavala et al. (2017, 2018). We adopt their counterpart identifications and various physical properties. Since deep 450 $\mu$m imaging is available ($1\sigma$ depth of 1.2 mJy), we limit our selection to the sources that have both 850 and 450 $\mu$m detections so the submillimeter detection is more robust. For the UDS field, Atacama Large Millimeter/submillimeter Array (ALMA) follow-up observations on a flux-limited sample of SCUBA-2 detected submillimeter sources have been carried out and the physical properties including their precise locations have been presented in Stach et al. (2018, 2019) and Dudzevičiūtė et al. (2020).

We first select SMGs that are at redshifts between 1.5 and 2.5. The choice of this redshift range is motivated by the fact that the observed wavelengths of JWST roughly corresponds to rest-frame UV for F115W and 1.6 $\mu$m for F444W filters, allowing us to study the distributions of the bulk of the stellar mass, and contrast this with young and less obscured star-forming regions. We then match these sources to the footprint of the CEERS and PRIMER data that were publicly released before the end of 2022 July. We find one and six SMGs within the PRIMER and CEERS footprint, respectively. The properties of our seven SMGs are provided in Table 1.

Overall, the median redshift of this sample is $2.1 \pm 0.2$, and the median 850 or 870 $\mu$m flux density ($S_{850/870}$) is $2.7 \pm 0.4$ mJy. Thus, the sample is consistent with the median redshift of the general SMG population at similar flux ranges (Chapman et al. 2005; Dudzevičiūtė et al. 2020) but lies at the fainter end compared to the typical SMG samples. As shown in Figure 1 they lie on the main sequence of star-forming galaxies at $z \sim 2$. In Figure 1 we also show the thumbnail JWST images of our sample SMGs. Note that the apparent extended radio emission on 850.025 suggests that the southern compact source could also be a counterpart of the SMG. However the much higher signal-to-noise ratio detection from the MIPS imaging suggests that the northern spiral galaxy is the counterpart. In addition, one recent JWST study has suggested that the southern compact source to be a $z \sim 4.5$ quiescent galaxy (Carnall et al. 2022). We therefore identify the northern spiral galaxy to be the JWST counterpart for 850.025.

### 2.2. HST Data

We make use of the publicly available CANDELS data (Grogin et al. 2011; Koekemoer et al. 2011), in particular the WFC3 F125W and F160W images, representing the reddest high-resolution imaging available prior to JWST, and the associated catalogs and estimated physical properties such as photometric redshifts (Galametz et al. 2013; Stefanon et al. 2017). As a check on the CANDELS astrometry, by cross-matching the CANDELS catalog to that of GAIA DR3 (Gaia Collaboration et al. 2021) we confirm that their coordinates are consistent with each other to the 0.″01 level.

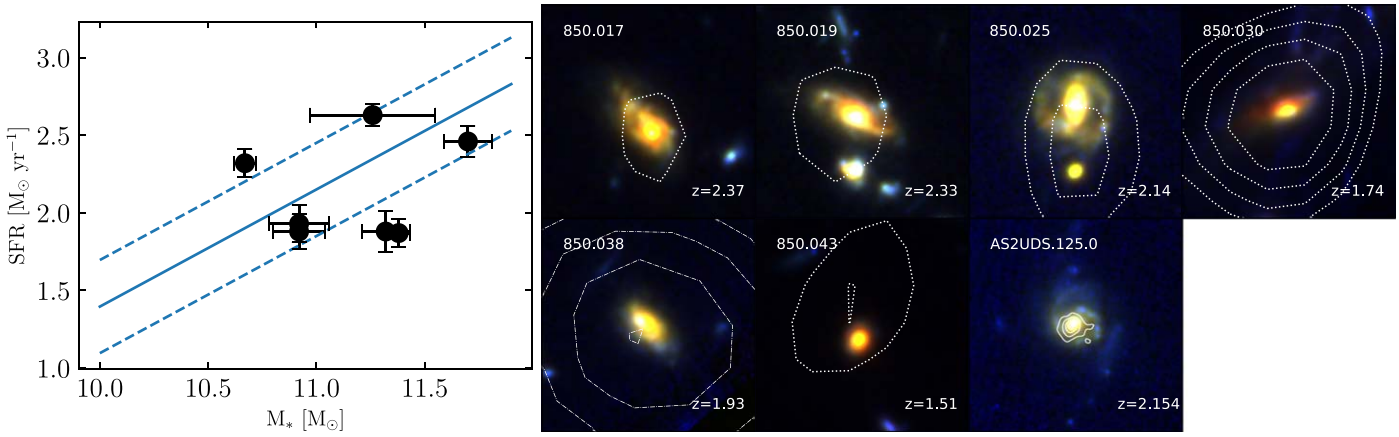


**Figure 1.** Left: stellar mass–SFR main sequence at $z = 2$ based on Speagle et al. (2014). Dashed lines show the range of $\pm 0.3$ dex scatter. The locations of the sample SMGs are marked as black data points. Our sample SMGs lie on the main sequence at $z \sim 2$. Right: thumbnail images of our sample SMGs with their IDs shown at the top left corner and their redshifts at bottom right, where photometric redshifts are shown to two decimal points and three decimal points for spectroscopic redshifts. The RGB images with 40 kpc on a side are made with NIRCam F115W, F277W, and F444W filters, except for 850.019 where the blue image is made with the F150W filter. The images are made with a linear stretch between 1% and 99.9%. The dotted contours show the VLA 1.4 GHz emissions with [3, 4, 5, 6] $\times \sigma$ levels, the dashed contours show the MIPS 24 $\mu$m emissions with [10, 13, 16, 19] $\times \sigma$ levels, and finally the smaller solid contours show the ALMA 870 $\mu$m continuum emissions with [5, 10, 15, 20] $\times \sigma$ levels. The JWST counterparts of the sample SMGs are robustly identified by VLA, MIPS, or ALMA.

### 2.3. JWST Data

The JWST data were taken as part of the ERS program CEERS (ID: 1345; Finkelstein et al. 2022) and the public GO program PRIMER (ID: 1837; PI: J. Dunlop). The wideband NIRCam imaging data taken using filters F115W, F150W, F200W, F277W, F356W, and F444W are obtained from the MAST archive. All the JWST data used in this paper can be found in MAST doi:10.17909/f8cx-p769. The publicly released version of the maps that we use all include stage 3 data products, which are based on images that are calibrated and resampled. Specifically, the calibration software versions 1.5.2 and 1.5.3 were used for CEERS and PRIMER data, respectively. The versions of the Calibration Reference Data System (CRDS) used were 11.13.1 and 11.16.3 for CEERS and PRIMER, respectively. The reference files used are jwst_0877.pmap and jwst_0942.pmap for CEERS and PRIMER, respectively. We examine the images in the following paragraphs and the results show that most of them are sufficient in quality for our purposes. We therefore adopt the public version and do not rerun data reduction.

We tie the astrometry of the NIRCam images to the publicly released CANDELS catalogs and find in general a pointing accuracy of $\sim 0\farcs1$, which is consistent with what has been reported by the JWST commissioning team (Rigby et al. 2022). We additionally find that the pointing offsets are significantly different between each of the two NIRCam modules, and the different offsets appear uncorrelated and it does not appear to be caused by the rotation parameters in the header. On the other hand, the detectors in the same module have consistent offsets and therefore no evidence of significant image distortion that would affect morphological analyses. Therefore, for our analyses we make astrometry corrections to the module where our sample SMGs are located.

To validate the photometry of NIRCam imaging we run SExtractor on all the available NIRCam images and compare the photometry between NIRCam and the published catalog from CANDELS. In particular we compare the NIRCam F150W measurements with those interpolated between WFC3 F140W and F160W measurements. We also compare NIRCam F356W and F444W photometry and that of IRAC Ch1 and Ch2 in the CANDELS catalog. In all three cases, for our sample SMGs, as well as most of the galaxies on the images that can be matched, the flux density measurements agree with each other.

We assess the depths of these NIRCam images by randomly positioning circular apertures in regions where no significant detection is obtained in SExtractor. We find that in general the $10\sigma$ depths for point sources[5] are about 27–29 AB magnitude, consistent with expectations given their exposure times, which based on the header are about 1–8 ks. Overall the data from PRIMER covering AS2UDS.125.0 are on the shallower side compared to those from CEERS that cover the rest of the sources, and the shorter-wavelength filters tend to be deeper by half to one magnitude than the longer-wavelength filters.

## 3. Analyses and Results

### 3.1. Galfit

We first employ GALFIT (Peng et al. 2010) to analyze the NIRCam images. For each image, we feed to GALFIT the science maps, weight maps, Nyquist sampled point spread functions (PSFs), and source masks. For the weight maps the publicly released versions are adopted but scaled in a way such that the standard deviation of the signal-to-noise ratio in blank regions is 1. We find typical scaling factors of about 2–6, depending on the filters. For PSFs, the pipeline produced maps have pixel scales of $0\farcs031$ and $0\farcs063$ for short- and long-wavelength filters, respectively, which are insufficient for Nyquist sampling the PSFs in most filters. In addition, it is often not possible to find many bright and unsaturated stars within the footprint to produce high-quality stacked PSFs. The undersampling issue can potentially be solved by making drizzled images that make use of subpixel dithering, but the issue of a lack of suitable stars does not have an immediate solution.

As a result, we adopt the following strategy that has often been used for HST images in similar conditions. We first use

[5] We use $0\farcs08$ and $0\farcs16$ radius apertures for short- and long-wavelength filters, respectively, following https://jwst-docs.stsci.edu/jwst-near-infrared-camera/nircam-performance/nircam-imaging-sensitivity.

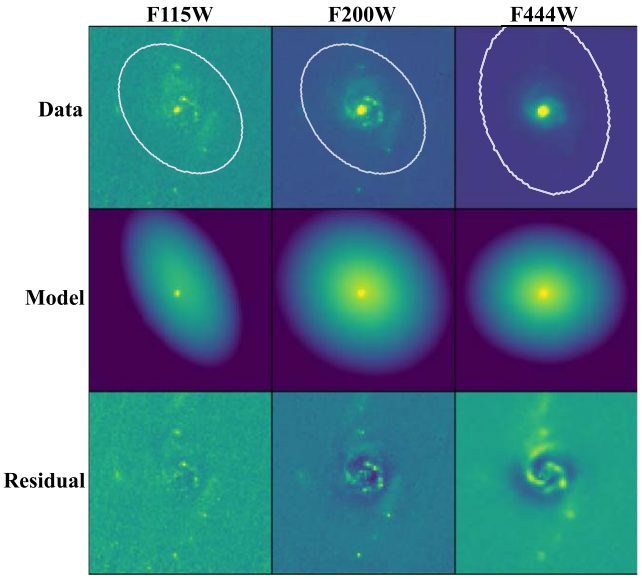


**Figure 2.** Top panels show the NIRCam science images with 5″ on a side centered at the ALMA confirmed SMG AS2UDS.125.0, where the white ellipses mark the source masks within which GALFIT modeling is performed. Middle and bottom panels show the model and residual maps produced by GALFIT. Example results of the three filters, F115W, F200W, and F444W, are shown in each column. We find at least two components, a bulge and a disk, are required to produce adequate fitting results in almost all filters of our sample SMGs, especially for F444W in which all sources need two components (Figure A1), suggesting stellar bulges are often present in SMGs.

the WEBBPSF software (Perrin et al. 2012) to generate synthetic PSFs for each filter, with an oversampling factor of 4. We then use GALFIT to convolve the synthetic PSFs with Gaussian profiles and fit them to the available nearby unsaturated stars. The resulting best-fit models are adopted as the Nyquist sampled PSFs. We find that the reduced $\chi^2$ values of the best-fit models vary source by source and filter by filter, ranging from close to 1 to about 100. Generally speaking those values are lower in longer-wavelength bands and they mainly depend on the brightness of the stars that we fit to. In most cases the central part of the PSF is well fitted by the best-fit models, and the $\chi^2$ values are mainly driven by the diffraction patterns in the outskirts. For source masks we adopt the aperture shapes suggested by SExtrator. The morphological parameters of these suggested apertures are also used as the first guess for Sérsic profile fittings in GALFIT.

For each science image we always start with a single Sérsic profile. We quickly find that a single Sérsic component often produces fits that are either not converged or large in $\chi^2$, and two components, a bulge and a disk in almost all cases, are required to significantly improve the fits, judging by the Bayesian information criterion. In one source, 850.025, we find that an additional bar component is also needed. Example results on AS2UDS.125.0 are shown in Figure 2, and full results on F444W, which trace the rest-frame *H* band given the redshifts of our sample SMGs, are shown in the Appendix (Figure A1 and Table A1). Overall, we find the median size of the bulge in the F444W filter is $0.7 \pm 1.0$ kpc (0.6–0.7–3.9 kpc for 14th–50th–86th percentiles) with a Sérsic index of $0.7 \pm 0.9$ (0.4–0.7–2.8 for 14th–50th–86th percentiles. In addition to needing two components, we also find that in the residual map structures mimicking spiral arms, tidal remnants, and clumps are often present (Figure A1). The frequent presence of spiral-arm-like structures (in at least half of the sample) is consistent with recent JWST studies on other SMG samples (Cheng et al. 2022; Wu et al. 2022). These structures seen on our sample SMGs suggest dynamical perturbations that could be caused by galaxy mergers or flybys. It is outside the scope of this Letter to quantitatively analyze these structures, but they suggest that JWST images can offer much more information than currently obtained. We also leave the GALFIT results in other filters to future works.

### 3.2. Curve of Growth

Since our analyses with GALFIT suggest that the optical and near-infrared morphology of the sample SMGs are complicated and can not be modeled by a single Sérsic profile, their overall half-light radii, or sizes, need to be estimated by other methods such as the curve-of-growth method. To prepare the images for the analyses we first made cutouts of about $10'' \times 10''$ and performed a sigma-clipped average sky subtraction for background removal. The apertures for the curve-of-growth analyses are constructed by adopting the positions of the peak pixel, corresponding to the bulge in most cases, as their centroids and the shapes of the apertures are according to those suggested by SExtractor. Thus, instead of using circular apertures we adopt elliptical apertures, and the length of the major axis is what is used for the curve of growth. Nearby unrelated sources are masked for the analyses.

In Figure 3 we show the curve-of-growth results, where the flux densities measured by each aperture size are divided by the total flux densities obtained from SExtractor. Images from a few filters for 850.019 and 850.038 are contaminated by uneven background at the edge of the images, leading to unreliable measurements so we do not report those results. Since the images are deep the errors of aperture photometry are small and the uncertainties of the curve of growth are dominated by the errors of the total flux density measurements.

We find in all cases sources have smaller sizes at longer wavelengths, and the median half-light radii along the major axis decrease from $0\farcs8 \pm 0\farcs2$ in F115W to $0\farcs5 \pm 0\farcs1$ in F444W. In particular, the median size ratio of $\langle R_{\rm e,F444W}/R_{\rm e,F150W}\rangle$ is found to be $0.6 \pm 0.1$, consistent with recent findings for general galaxy populations at the redshift range of the sample SMGs (Suess et al. 2022). We provide half-light radii in each filter for each source in Table 1. Note that one typical concern of using the curve-of-growth analyses to derive sizes is that it is not straightforward to take into account the broadening effect caused by the PSFs. This becomes a more serious issue when the source sizes are close to those of the PSFs. However as shown in Figure 3 most of our sources are much more extended than the PSFs, except 850.043. By forcing GALFIT to perform single Sérsic component fitting we determine the true sizes of 850.043 to be smaller by 30% at most, which occurs in F444W, and the differences are much smaller in other filters. However, since we mainly discuss median values one single source does not affect our conclusions significantly.

## 4. Discussion and Summary

In this Letter we analyze morphology and sizes of a sample of seven SMGs at $z \sim 2$ using JWST NIRCam imaging. Via GALFIT analyses we report detection of bulge components in all the sample SMGs, most prominently in the F444W filter, which in principle traces stellar distributions at the redshift range of

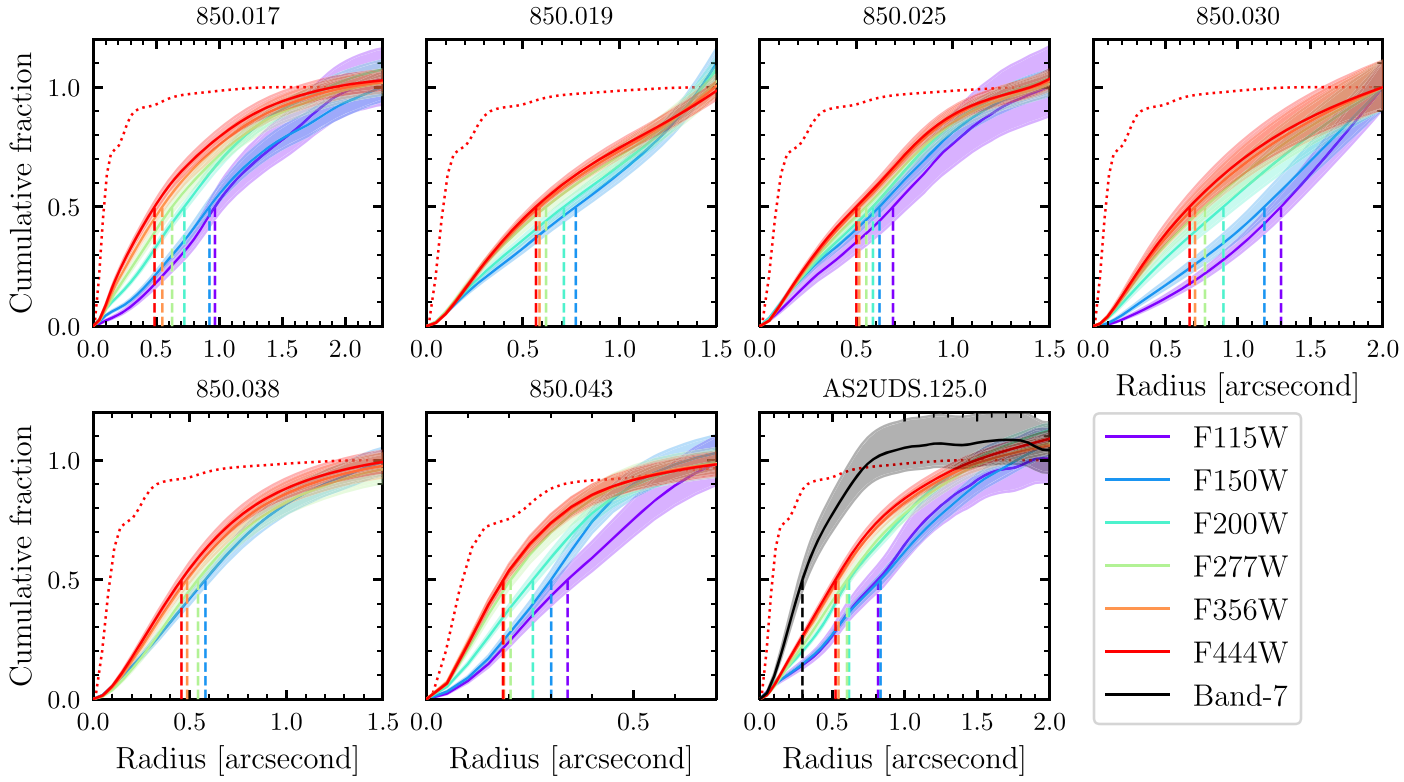


**Figure 3.** Cumulative fractions of integrated flux densities measured from NIRCam on all seven sample SMGs as well as those from ALMA band 7 on AS2UDS.0125.0. Vertical lines with corresponding colors mark the half-light radii in the major axis, and the dotted lines show the results of PSFs at F444W. In all cases, half-light radii are smaller at longer wavelengths. It is also evident that bulges, despite presenting in many sources, do not dominate the total flux densities.

our sample. The detection of bulges is enabled thanks to the superior sensitivity and spatial resolution of JWST. Indeed, by examining previous HST *H*-band imaging and morphological analyses on our sample SMGs by van der Wel et al. (2014), hints of a bulge component have already existed, but the much lower signal-to-noise detection together with poorer spatial resolution means that Sérsic profile fitting can yield adequate results with just one single component. In two cases (850.019 and 850.025) the fitting of the HST images already leans toward the bulge as suggested by the reported Sérsic indices ($3.1 \pm 0.2$ and $3 \pm 0.2$, respectively), and in two cases (850.030 and AS2UDS.125.0) bad fits were reported, suggesting complicated morphology confirmed by the JWST imaging (Figure A1). We show more comparisons to the HST results in a later paragraph.

The residual images produced from GALFIT are also informative. Structures mimicking spiral arms can been seen in most cases, and one SMG (850.025) requires a bar component for the fitting. Spiral-arm-like structures have also been reported in recent JWST studies of other SMG samples (Cheng et al. 2022; Wu et al. 2022). These structures are consistent with those suggested by recent high-resolution ALMA observations on dust and gas morphologies of SMGs, although those are in the central regions so are on a smaller scale (Gullberg et al. 2019; Hodge et al. 2019; Tsukui & Iguchi 2021). However, the spiral-arm-like structures revealed by JWST can be perceived asymmetric or perturbed in many cases and two SMGs (850.019 and 850.030) appear to be undergoing a merger. Indeed, based on the photometric redshifts reported in the CANDELS catalogs (Santini et al. 2015; Stefanon et al. 2017), six out of the seven sample SMGs have at least one nearby source with consistent redshifts as those of the corresponding SMGs at a projected distance of 2″–5″, so ∼15–45 kpc. This evidence suggests that the sample SMGs are experiencing dynamical interactions with nearby sources, which may be responsible for the triggering of their star formation (e.g., Chen et al. 2015; Gomez-Guijarro et al. 2018). Similar studies with JWST on a much larger SMG sample will allow determinations of the relative fractions of various morphological types such as a major merger, a minor merger, and an isolated disk with or without bars, and these results will provide powerful constraints on theoretical models.

We also report sizes of our sample SMGs in Section 3.2. In Figure 4 we show a compilation of all results that are converted into angular physical sizes based on their redshifts. We find median sizes ($R_e$) of $7.0 \pm 1.6$ kpc, $6.5 \pm 1.0$ kpc, $5.6 \pm 0.7$ kpc, $5.1 \pm 0.6$ kpc, $4.6 \pm 0.4$ kpc, and $4.3 \pm 0.4$ kpc in the F115W, F150W, F200W, F277W, F356W, and F444W bands, respectively. The reported size measurements of our sample SMGs based on HST F125W and F160W (van der Wel et al. 2014) are also shown, which are consistent with the JWST measurements at similar wavelengths. The sizes of our sample SMGs at F150W are however marginally larger than the reported HST *H*-band sizes for general SMG samples (Chen et al. 2015; Lang et al. 2019), by a factor of about $50\% \pm 40\%$. While the difference is not significant, this suggests that our sample may be somehow biased large in size. This suggestion may help explain a similar amount of difference on the reported F444W sizes between our measurements and those of Cheng et al. (2022), who found F444W sizes of about 3 kpc (corrected for lensing) based on two ALMA identified SMGs in the SMACS J0723 field.

The sizes based on NIRCam imaging appear to be significantly larger than those reported based on ALMA

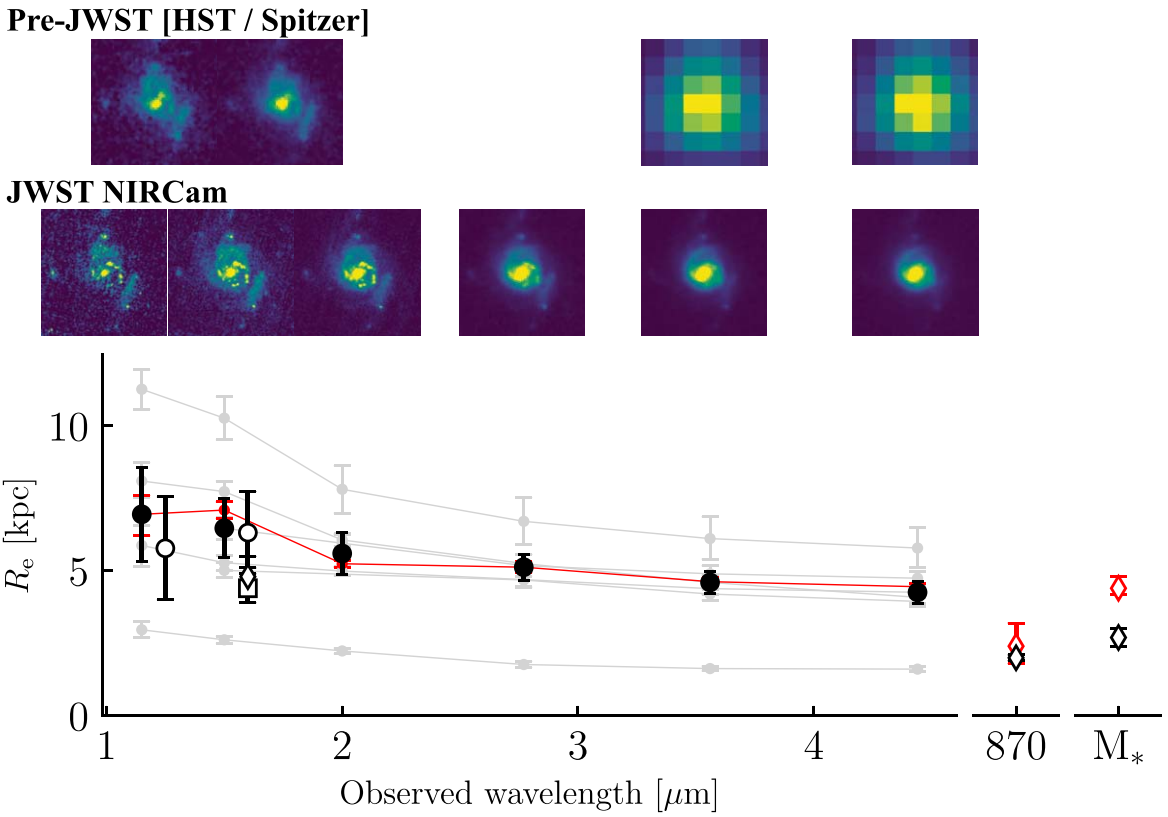


**Figure 4.** Half-light radii in observed wavelengths of our sample SMGs are shown in gray points, where measurements of the same source are connected by lines and those from AS2UDS.125.0 are explicitly marked in red. The median values of each wave band are shown in larger black points with bootstrapped uncertainties. Empty circles show size measurements of our sample SMGs based on the published HST results in the *J* and *H* bands (van der Wel et al. 2014), empty squares show *H*-band sizes of SMGs reported by Chen et al. (2015), and empty diamonds show sizes measured by Lang et al. (2019), where the 870 $\mu$m sizes and stellar mass sizes are also shown. At the top we show cutout images with 4″ on a side from HST, Spitzer, and JWST of one of our sample SMGs confirmed by ALMA, AS2UDS.125.0, and these cutouts are aligned vertically roughly to the wavelengths shown in the *x*-axis below.

observations at 870 $\mu$m in one of our sample SMGs as well as on other samples of SMGs (Simpson et al. 2015; Hodge et al. 2016; Gullberg et al. 2019; Lang et al. 2019; Tadaki et al. 2020), which are mostly below 2 kpc. If we account for the potential size bias of our sample the median F444W size would have been $3.0 \pm 0.3$ kpc, still not smaller than the submillimeter sizes and consistent with the stellar sizes of SMGs reported by Lang et al. (2019), who used $J - H$ colors to infer stellar mass distributions. Adopting the submillimeter size reported by Lang et al. (2019), our measured submillimeter-to-F444W size ratio of $0.5 \pm 0.1$ is also consistent with that inferred from an IRAC study on lensed SMGs (Sun et al. 2021). Our results suggest that while stellar bulges are in active formation phase in SMGs, the total stellar masses are yet to be dominated by bulges; thus, the stellar mass sizes, in our case inferred from F444W sizes, are still larger than the star-forming bulges. Our results are in contrast with recent predictions from certain hydrodynamical simulations, which suggest smaller stellar mass sizes than submillimeter sizes in the mass range of our sample SMGs (Cochrane et al. 2019; Popping et al. 2022).

Our results demonstrate the power of JWST in understanding the stellar distributions of heavily dust-obscured galaxies like SMGs. More in-depth analyses on JWST imaging on larger SMG samples should allow us to start addressing issues such as the correlations between sizes and various physical parameters and the properties of clumps and spiral arms. Combining morphological studies using JWST and ALMA would unveil fresh details with regards to how exactly the buildup of stellar bulges in massive galaxies took place at cosmic noon.

We acknowledge the referee for a helpful report that has improved the manuscript. C.C.C., Q.-N.H, C.-L.L., and Y.-H.L acknowledge support from the National Science and Technology Council of Taiwan (NSTC 109-2112-M-001-016-MY3 and 111-2112-M-001-045-MY3). I.R.S. acknowledges support from STFC (ST/T000244/1). This work is based in part on observations made with the NASA/ESA/CSA James Webb Space Telescope. The data were obtained from the Mikulski Archive for Space Telescopes at the Space Telescope Science Institute, which is operated by the Association of Universities for Research in Astronomy, Inc., under NASA contract NAS 5-03127 for JWST. These observations are associated with programs ERS 1345 and GO 1837. The authors acknowledge the CEERS and PRIMER teams for developing their observing program with a zero-exclusive-access period. This Letter makes use of the following ALMA data: ADS/ JAO. ALMA#2015.1.01528.S and 2017.1.01027.S. ALMA is a partnership of ESO (representing its member states), NSF (USA) and NINS (Japan), together with NRC (Canada), MOST and ASIAA (Taiwan), and KASI (Republic of Korea), in cooperation with the Republic of Chile. The Joint ALMA Observatory is operated by ESO, AUI/NRAO and NAOJ.

This paper was written in a time when the world appears to be in a period of turmoil. We wish peace and stability would soon be upon us all.

*Facilities:* JWST(NIRCam), HST(WFC3), JCMT(SCUBA-2), Spitzer(IRAC, MIPS), ALMA.

*Software:* astropy (Astropy Collaboration et al. 2018), SExtractor (Bertin & Arnouts 1996), Galfit (Peng et al. 2002, 2010), WebbPSF (Perrin et al. 2012).

## Appendix

In this appendix we plot the full GALFIT results in the F444W filter in Figure A1 and provide sizes and Sérsic indices in Table A1.

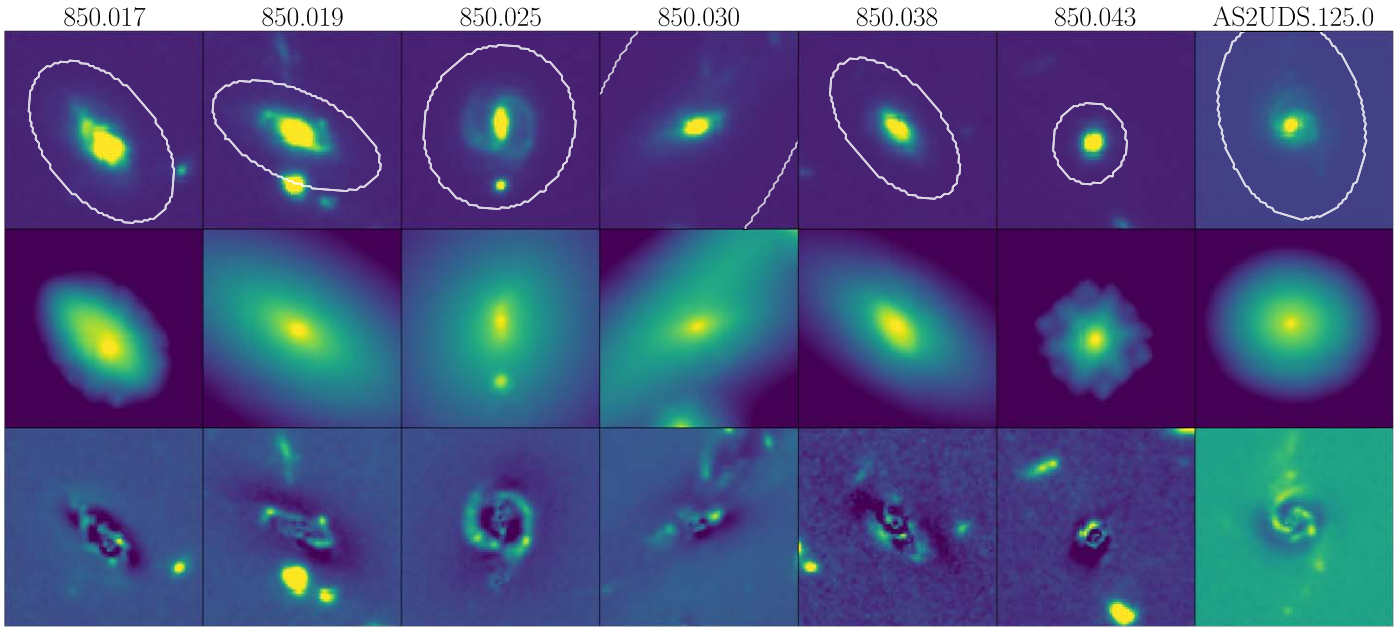


**Figure A1.** Similar to Figure 2, but here we show the GALFIT results only in the F444W filter but on all sample SMGs.

**Table A1**
Results of Sérsic Fittings Using the F444W Images

| ID | Disk | | Bulge | |
|---|---|---|---|---|
| | $R_e$ (kpc) | $n$ | $R_e$ (kpc) | $n$ |
| 850.017 | $5.43 \pm 0.05$ | $0.44 \pm 0.01$ | $0.68 \pm 0.02$ | $2.32 \pm 0.10$ |
| 850.019 | $7.33 \pm 0.60$ | $2.14 \pm 0.28$ | $0.81 \pm 0.04$ | $0.69 \pm 0.11$ |
| 850.025 | $10.06 \pm 0.56$ | $2.54 \pm 0.07$ | $0.70 \pm 0.01$ | $0.61 \pm 0.04$ |
| 850.030 | $23.91 \pm 0.60$ | $0.61 \pm 0.02$ | $3.91 \pm 0.03$ | $2.73 \pm 0.02$ |
| 850.038 | $3.37 \pm 0.02$ | $0.33 \pm 0.01$ | $4.50 \pm 0.21$ | $3.82 \pm 0.10$ |
| 850.043 | $1.49 \pm 0.22$ | $1.33 \pm 0.03$ | $0.64 \pm 0.01$ | 0.05[a] |
| AS2UDS.125.0 | $4.31 \pm 0.03$ | $0.79 \pm 0.01$ | $0.62 \pm 0.01$ | 0.5[a] |

**Note.**
[a] Sérsic indices are fixed in the fitting to ensure converged results.

## ORCID iDs

Chian-Chou Chen (陳建州) https://orcid.org/0000-0002-3805-0789
Zhen-Kai Gao https://orcid.org/0000-0003-1262-7719
Cheng-Lin Liao https://orcid.org/0000-0002-5247-6639
Ian Smail https://orcid.org/0000-0003-3037-257X
Wei-Hao Wang https://orcid.org/0000-0003-2588-1265
Yu-Jan Wang https://orcid.org/0000-0001-6768-3422

## References

Astropy Collaboration, Price-Whelan, A. M., Sipőcz, B. M., et al. 2018, AJ, 156, 123
Barger, A. J., Cowie, L. L., Sanders, D. B., et al. 1998, Natur, 394, 248
Baugh, C. M., Lacey, C. G., Frenk, C. S., et al. 2005, MNRAS, 356, 1191
Bertin, E., & Arnouts, S. 1996, A&AS, 117, 393
Blain, A. W., Smail, I., Ivison, R. J., Kneib, J., & Frayer, D. T. 2002, PhR, 369, 111
Calistro Rivera, G., Hodge, J. A., Smail, I., et al. 2018, ApJ, 863, 56
Carnall, A. C., McLeod, D. J., McLure, R. J., et al. 2022, arXiv:2208.00986
Casey, C. M., Narayanan, D., & Cooray, A. 2014, PhR, 541, 45
Chang, Y.-Y., Ferraro, N., Wang, W.-H., et al. 2018, ApJ, 865, 103
Chapman, S. C., Blain, A. W., Smail, I., & Ivison, R. J. 2005, ApJ, 622, 772
Chen, C.-C., Harrison, C. M., Smail, I., et al. 2020, A&A, 635, A119
Chen, C.-C., Liao, C.-L., Smail, I., et al. 2022, ApJ, 929, 159
Chen, C.-C., Smail, I., Swinbank, A. M., et al. 2015, ApJ, 799, 194
Cheng, C., Yan, H., Huang, J.-S., et al. 2022, ApJL, 936, L19
Cochrane, R. K., Hayward, C. C., Anglés-Alcázar, D., et al. 2019, MNRAS, 488, 1779
Cowley, W. I., Lacey, C. G., Baugh, C. M., & Cole, S. 2015, MNRAS, 446, 1784
Danielson, A. L. R., Swinbank, A. M., Smail, I., et al. 2017, ApJ, 840, 78
Davé, R., Finlator, K., Oppenheimer, B. D., et al. 2010, MNRAS, 404, 1355
Dudzevičiūtė, U., Smail, I., Swinbank, A. M., et al. 2020, MNRAS, 494, 3828
Finkelstein, S. L., Bagley, M. B., Arrabal Haro, P., et al. 2022, arXiv:2207.12474
Fujimoto, S., Ouchi, M., Kohno, K., et al. 2018, ApJ, 861, 7
Gaia Collaboration, Brown, A. G. A., Vallenari, A., et al. 2021, A&A, 649, A1
Galametz, A., Grazian, A., Fontana, A., et al. 2013, ApJS, 206, 10
Geach, J. E., Dunlop, J. S., Halpern, M., et al. 2017, MNRAS, 465, 1789
Gomez-Guijarro, C., Toft, S., Karim, A., et al. 2018, ApJ, 856, 121
Grogin, N. A., Kocevski, D. D., Faber, S. M., et al. 2011, ApJS, 197, 35
Gullberg, B., Smail, I., Swinbank, A. M., et al. 2019, MNRAS, 490, 4956
Hayward, C. C., Behroozi, P. S., Somerville, R. S., et al. 2013, MNRAS, 434, 2572
Hodge, J. A., Smail, I., Walter, F., et al. 2019, ApJ, 876, 130
Hodge, J. A., Swinbank, A. M., Simpson, J. M., et al. 2016, ApJ, 833, 103
Hughes, D. H., Serjeant, S., Dunlop, J., et al. 1998, Natur, 394, 241
Ikarashi, S., Ivison, R. J., Caputi, K. I., et al. 2015, ApJ, 810, 133
Koekemoer, A. M., Faber, S. M., Ferguson, H. C., et al. 2011, ApJS, 197, 36
Lagos, C. d. P., da Cunha, E., Robotham, A. S. G., et al. 2020, MNRAS, 499, 1948
Lang, P., Schinnerer, E., Smail, I., et al. 2019, ApJ, 879, 54
Lilly, S. J., Eales, S. A., Gear, W. K. P., et al. 1999, ApJ, 518, 641
Madau, P., & Dickinson, M. 2014, ARA&A, 52, 415
Miller, T. B., van Dokkum, P., & Mowla, L. 2022, arXiv:2207.05895
Mortlock, A., Conselice, C. J., Hartley, W. G., et al. 2013, MNRAS, 433, 1185
Nelson, E. J., van Dokkum, P. G., Forster Schreiber, N. M., et al. 2016, ApJ, 828, 27
Peng, C. Y., Ho, L. C., Impey, C. D., & Rix, H.-W. 2002, AJ, 124, 266
Peng, C. Y., Ho, L. C., Impey, C. D., & Rix, H.-W. 2010, AJ, 139, 2097
Perrin, M. D., Soummer, R., Elliott, E. M., Lallo, M. D., & Sivaramakrishnan, A. 2012, Proc. SPIE, 8442, 84423D
Planck Collaboration, Aghanim, N., Akrami, Y., et al. 2020, A&A, 641, A6
Popping, G., Pillepich, A., Calistro?Rivera, G., et al. 2022, MNRAS, 510, 3321
Rigby, J., Perrin, M., McElwain, M., et al. 2022, arXiv:2207.05632
Santini, P., Ferguson, H. C., Fontana, A., et al. 2015, ApJ, 801, 97
Simpson, J. M., Smail, I., Swinbank, A. M., et al. 2015, ApJ, 799, 81
Smail, I., Ivison, R. J., & Blain, A. W. 1997, ApJL, 490, L5
Speagle, J. S., Steinhardt, C. L., Capak, P. L., & Silverman, J. D. 2014, ApJS, 214, 15
Spilker, J. S., Marrone, D. P., Aravena, M., et al. 2016, ApJ, 826, 112
Stach, S. M., Dudzeviciute, U., Smail, I., et al. 2019, MNRAS, 487, 4648
Stach, S. M., Smail, I., Swinbank, A. M., et al. 2018, ApJ, 860, 161
Stefanon, M., Yan, H., Mobasher, B., et al. 2017, ApJS, 229, 32
Suess, K. A., Bezanson, R., Nelson, E. J., et al. 2022, ApJL, 937, L33
Suess, K. A., Kriek, M., Price, S. H., & Barro, G. 2019, ApJ, 877, 103
Sun, F., Egami, E., Rawle, T. D., et al. 2021, ApJ, 908, 192
Swinbank, A. M., Smail, I., Chapman, S. C., et al. 2010, MNRAS, 405, 234
Tadaki, K.-i., Belli, S., Burkert, A., et al. 2020, ApJ, 901, 74
Toft, S., Smolcic, V., Magnelli, B., et al. 2014, ApJ, 782, 68
Tsukui, T., & Iguchi, S. 2021, Sci, 372, 1201
van der Wel, A., Franx, M., van Dokkum, P. G., et al. 2014, ApJ, 788, 28
Wu, Y., Cai, Z., Sun, F., et al. 2022, arXiv:2208.08473
Zavala, J. A., Aretxaga, I., Dunlop, J. S., et al. 2018, MNRAS, 475, 5585
Zavala, J. A., Aretxaga, I., Geach, J. E., et al. 2017, MNRAS, 464, 3369